PHYSICAL REVIEW B **105**, 165402 (2022)

Tunneling properties in α-T_3 lattices: Effects of symmetry-breaking terms

S. M. Cunha,[1,2,*] D. R. da Costa,[2,3] J. Milton Pereira, Jr.,[2] R. N. Costa Filho,[2] B. Van Duppen,[1] and F. M. Peeters[1]

[1] *Department of Physics, University of Antwerp, Groenenborgerlaan 171, B-2020 Antwerp, Belgium*
[2] *Departamento de Física, Universidade Federal do Ceará, Campus do Pici, Fortaleza, Ceará, Brazil*
[3] *Key Laboratory for Micro/Nano Optoelectronic Devices of Ministry of Education & Hunan Provincial Key Laboratory of Low-Dimensional Structural Physics and Devices, School of Physics and Electronics, Hunan University, Changsha 410082, China*

(Received 23 November 2021; revised 4 March 2022; accepted 18 March 2022; published 1 April 2022)

The α-T_3 lattice model interpolates a honeycomb (graphene-like) lattice and a T_3 (also known as dice) lattice via the parameter α. These lattices are made up of three atoms per unit cell. This gives rise to an additional dispersionless flat band touching the conduction and valence bands. Electrons in this model are analogous to Dirac fermions with an enlarged pseudospin, which provides unusual tunneling features like omnidirectional Klein tunneling, also called super-Klein tunneling (SKT). However, it is unknown how small deviations in the equivalence between the atomic sites, i.e., variations in the α parameter, and the number of tunnel barriers changes the transmission properties. Moreover, it is interesting to learn how tunneling occurs through regions where the energy spectrum changes from linear with a middle flat band to a hyperbolic dispersion. In this paper we investigate these properties, its dependence on the number of square barriers and the α parameter for either gapped and gapless cases. Furthermore, we compare these results to the case where electrons tunnel from a region with linear dispersion to a region with a bandgap. In the latter case, contrary to tunneling through a potential barrier, the SKT is no longer observed. Finally, we find specific cases where transmission is allowed due to a symmetry breaking of sublattice equivalence.

DOI: 10.1103/PhysRevB.105.165402

I. INTRODUCTION

The probability for a particle to cross potential barriers even through a classically forbidden region with a tiny probability is a quantum phenomenon. This counterintuitive aspect of the transmission takes place when a particle, with some probability, can create a "tunnel" that enables it to traverse a potential barrier even when it is higher than the particle energy. Although such tunneling is not expected in a classical particle dynamics approach, an analogous effect called evanescent wave coupling takes place in optics, in which an electromagnetic wave is transmitted through a region where the solution of the corresponding wave equation is exponentially decaying. In quantum mechanics, likewise, the tunneling of a particle can be said to arise due to the coupling of the propagating solutions of Schrödinger's equation at either sides of the potential barrier with decaying solutions in the barrier region, leading to nonzero transmission probabilities [1].

However, counterintuitive effects emerge in the tunneling of relativistic particles [2–5]. One example is the total transmission of relativistic particles through large potential steps at certain values of momentum, which is known as the *Klein paradox* [3–5]. Although it was first described by Klein, experimental realization of a similar effect known as the "Klein tunneling" (KT), an usual tunneling property characterized by the suppression of backscattering by potential barriers [6–8], has only recently been observed [9–12] following the isolation of stable-single layer (graphene) and bilayer carbon crystals where the carbon atoms are arranged on a honeycomb lattice (HCL) [6,13–15]. Since electrons in graphene at low energy are well described by the two-dimensional (2D) massless Dirac equation, i.e., the Dirac-Weyl equation with pseudospin $S = 1/2$, graphene boosted the exploration of fundamental research in 2D materials [16], bridging condensed matter physics, relativistic quantum mechanics, and quantum field theory, resulting in the probing of interesting relativistic predictions, such as KT [6,9–12,15] and Zitterbewegung [17–20].

The KT observed in graphene is strongly related to the conservation of chirality for carriers in this material and the nature of its pseudospin [21,22]. Instigated by such unusual properties lying on the 2D panorama, the search for new graphene-based materials has been intensified in the past two decades. Examples of these 2D materials is T_3 or dice lattice [23], Lieb [24], and Kagome [25] lattices. These lattices result from altering the HCL of graphene by adding an atom at the center of the hexagons of the unit cell [23–30]. As a consequence, the charge carriers are described as enlarged pseudospin Dirac fermions [23,28,31–33] and a flatband appears touching the top of the valence and the bottom of the conduction linear bands in the energy spectrum [34,35]. This flatband has important and unusual effects on the electronic properties due to its dispersionless nature [33–41].

The α-T_3 model interpolates between the HCL and the dice lattice by varying the parameter $\alpha = \tan\theta$, corresponding to the strength between the HCL and the central site, from $\alpha = 0$ to $\alpha = 1$, respectively, with the limiting cases of the HCL ($\theta = 0$) and the dice lattice ($\theta = \pi/4$) [34,38–41]. Unlike graphene, charge carriers in α-T_3 lattices are described as massless Dirac fermions only in the limiting

---

[*] sofiacunha@fisica.ufc.br

case $\alpha = 1$, i.e., dice lattice. For certain energy conditions, it presents an angular independent Klein tunneling through rectangular electrostatic barriers called super-Klein tunneling (SKT) [32,41]. In addition, an extraordinary Snell law is found allowing a refracted particle beam to be focused at one point, such as occurs in a Veselago lens [42–44]. Furthermore, there is a general trend of enhanced transmission when increasing the α parameter [32,41,45]. Moreover, in the case of the dice lattice the tunneling is less sensitive to the number of barriers for certain values of energy [46], whereas for graphene the number of barriers strongly affects the tunneling [47].

Nonetheless, for practical electronic applications such as the fabrication of quantum information devices the creation of a bandgap is necessary. It was demonstrated that an additional mass term in α-T_3 systems distorts the linear bands around the Dirac cone and produces an energy gap with a third band in it which could be flat or dispersive [39,40]. In the present paper and using the theoretical formalism developed in Ref. [48], we theoretically study the emergence of SKT and under what conditions this phenomena is affected when the equivalence between the sublattices is broken and by increasing the number of barriers. We find that as a consequence of the enlarged pseudospin and the symmetry between the three sublattices, for the dice lattice increasing the number of barriers effects less the transmission properties for electrons with incident energy around half the height of the potential and omnidirectional tunneling is observed regardless the number of barriers. Additionally, we investigate the role of the location of the flat band in the transmission properties of charge carriers across potential barriers for particular values of α when different symmetry-breaking terms are taken into account. In both cases we find that small deviations in the symmetry between the sublattices, followed by modifications in the electronic band structures as discussed in Ref. [48], result in strong modifications on the nature of wave vectors inside the barriers, consequently, affecting the tunneling properties of charge carriers. Subsequently, we analyze the transmission of chiral electrons in α-T_3 lattice through a region where the electronic spectrum changes from linear dispersion to hyperbolic dispersion with a bandgap and we compare these results with those for HCL [49]. We highlight that KT is prevented to take place and the transmission probability is less than 1 for all values of θ for perpendicular incident angles, although the peaks of resonant transmission becomes smooth as θ increases and a perfect transmission is observed for larger values of incident angle.

This paper is organized as follows. In Sec. II, we discuss the electronic properties of charge carriers in α-T_3 lattices, and how this is affected by small deviations in the atomic equivalence between the sites. The consequences of the presence of mass terms on the energy spectrum are discussed in Sec. III. In Sec. IV, we develop the transfer-matrix approach to analyze the tunneling of Dirac fermions in α-T_3 lattices through a 1D periodic potential. In Secs. V and VI, we discuss the transmission properties of massless fermions and the effects of symmetry-breaking on the tunneling properties. In Sec. VII, we investigate the tunneling through spatial regions where the energy spectrum of fermions in α-T_3 changes from linear to hyperbolic dispersion. Conclusions are presented in Sec. VIII.

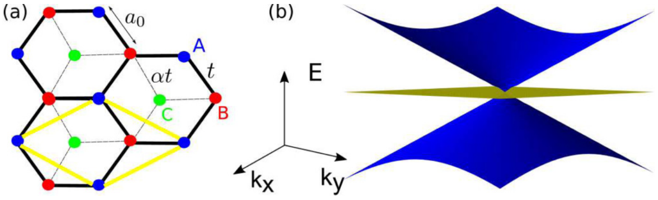

FIG. 1. (a) Illustration of the α-T_3 lattice with three atomic sites (A, B, and C) per unit cell (yellow rhombus) is shown. $\alpha = 0$ and $\alpha = 1$ limits correspond to HC (graphene-like) and dice lattices. $A - B$ and $B - C$ sites are connected by the hopping amplitude t and αt, respectively. (b) Low-energy spectrum of massless Dirac fermions in the α-T_3 lattice, composed by a linear dispersion and a flat band.

II. FERMIONS IN α-T_3 LATTICE

The low-energy Hamiltonian for the α-T_3 model, a crystallographic lattice composed by three atoms per unit cell as illustrated in Fig. 1(a), around the K point in the first Brillouin zone can be written as

$$\hat{H}_{\text{kin}} = \begin{pmatrix} 0 & f_k(\tau)\cos\theta & 0 \\ f_k^*(\tau)\cos\theta & 0 & f_k(\tau)\sin\theta \\ 0 & f_k^*(\tau)\sin\theta & 0 \end{pmatrix}, \tag{1}$$

where $\theta = \tan^{-1}\alpha$ is the angle that provides a continuous evolution from the honeycomb graphene-like ($\alpha = 0$) to the dice ($\alpha = 1$) lattice via the parameter α. The tuning parameter is proportional to the strength of the coupling between B sites with the additional atoms C at the center of the HCL, as shown in Fig. 1(a), and the other two atomic sites A and B are connected by the hopping parameter t. In Eq. (1) we defined the function $f_k(\tau) = v_F(\tau k_x - ik_y)$, with $v_F = 3a_0t/2\hbar$ the Fermi velocity, a_0 the lattice constant, $\vec{k} = (k_x, k_y)$ the wave vector, and $\tau = +1(-1)$ is the valley index for the K and K' valleys, respectively. In the absence of external potentials, the eigenstates of the Hamiltonian are given by

$$|\Psi_\pm\rangle = \begin{pmatrix} \cos\theta e^{i\phi_k} \\ \pm 1 \\ \sin\theta e^{-i\phi_k} \end{pmatrix}, \tag{2}$$

with eigenvalues $E_\pm = \pm\hbar v_F k$, where $+(-)$ indicates the conduction and valence bands, respectively, resulting in graphene-like conical energy bands. The angle $\phi_k = \tan^{-1}(k_y/k_x)$ corresponds to the polar angle associated with the momentum-vector. In additional to the linear dispersion, a third energy band, with eigenvalue $E = 0$, is also found, being a highly degenerate state, as shown in Fig. 1(b). It is associated to the flat-band state

$$|\Psi_0\rangle = \begin{pmatrix} \cos\theta e^{i\phi_k} \\ 0 \\ \sin\theta e^{-i\phi_k} \end{pmatrix}, \tag{3}$$

with eigenvalues that do not depend on the θ parameter, which affects only the eigenstates.

III. INTRODUCTION OF BAND-GAP

The degeneracy observed at $E = 0$ in the energy spectrum shown in Fig. 1(b) is lifted when the equivalence between the three sublattices is broken, and a gap is introduced into

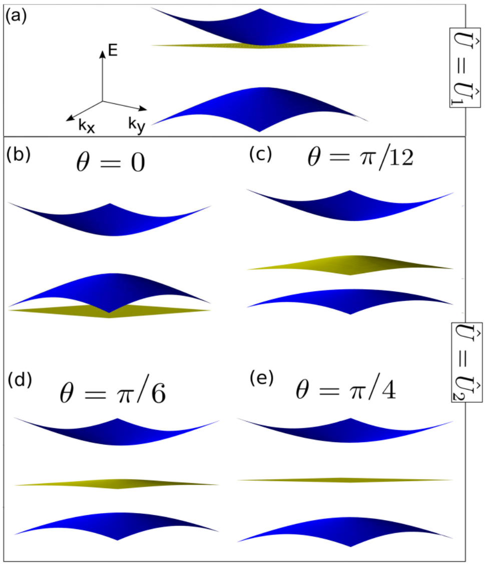

FIG. 2. Energy spectrum of Dirac fermions around the K point for different values of the parameter θ in the α-T_3 lattices when (a) the sublattice symmetry-breaking term $\hat{U}=\hat{U}_1$ is taken in Eq. (4), and for the symmetry-breaking term $\hat{U}=\hat{U}_2$ when (b) $\theta=0$ (graphene-like), (c) $\theta=\pi/12$, (d) $\theta=\pi/6$, and (e) $\theta=\pi/4$ (dice).

the energy spectrum. In general, we can include this in the Hamiltonian by a term $\hat{U}$, as follows:

$$\hat{H}=\hat{H}_{\text{kin}}+\Delta\hat{U}, \tag{4}$$

with the kinetic term $\hat{H}_{\text{kin}}$ given by Eq. (1), and Δ measures the strength of the sublattice symmetry breaking. We consider two different forms of the $\hat{U}$ matrix, respectively, given by

$$\hat{U}_1=\begin{pmatrix}1&0&0\\0&-1&0\\0&0&1\end{pmatrix},\quad \hat{U}_2=\begin{pmatrix}1&0&0\\0&-1&0\\0&0&-3\end{pmatrix}. \tag{5}$$

The effects of the inclusion of the terms $\hat{U}_1$ and $\hat{U}_2$ on the energy spectrum are shown in Figs. 2(a)–2(e), respectively.

The solution of $\hat{H}\Psi=E\Psi$ when $\hat{U}=\hat{U}_1$ gives the eigenenergies

$$E_0=\Delta,\quad E=\pm\sqrt{\Delta^2+\hbar^2v_{\text{F}}^2k^2}. \tag{6}$$

Correspondingly, the wave functions in this case are given by

$$|\psi_0\rangle=\begin{pmatrix}\cos\theta e^{i\phi_k}\\0\\\sin\theta e^{-i\phi_k}\end{pmatrix},\quad |\psi_\pm\rangle=\begin{pmatrix}\alpha\cos\theta e^{-i\phi_k}\\\gamma\\\alpha\sin\theta e^{i\phi_k}\end{pmatrix}, \tag{7}$$

where $\alpha=\sqrt{E+\Delta}$ and $\gamma=\sqrt{E-\Delta}$.

According to Eq. (6), one obtains an energy spectrum with a band-gap opening of 2Δ. It is worth mentioning that the format of $\hat{U}_2$ in Eq. (5) was chosen in order that both sublattice symmetry-breaking terms $\hat{U}_1$ and $\hat{U}_2$ give rise to the same 2Δ band-gap opening. This results in massive Dirac fermions with an effective mass defined as $m=\Delta/v_F^2$. Since Eq. (6) does not depend on the parameter θ, the energy spectrum remains the same for all α-T_3 lattices, as shown in Fig. 2(a). Moreover, as long as the equivalence between the sites A and C is maintained, the flat band is shifted and touches only the bottom of the conduction band. Notice that now the bottom of the conduction band and the top of the valence band are hyperbolic in k.

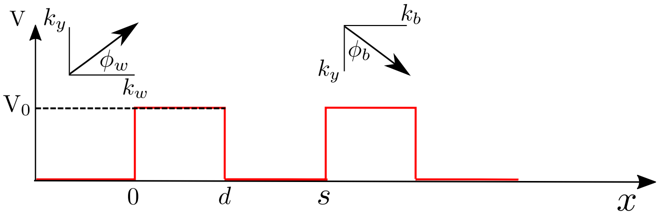

FIG. 3. Schematic illustration (see top insets) of the wave vectors in the tunneling process through an electrostatic finite superlattice formed by rectangular barriers of height V_0 and width d. The well width, i.e., the interbarrier distance, is $s-d$.

When we assume $\hat{U}=\hat{U}_2$ in Eq. (4), the energy dispersion relation is obtained from a nonlinear equation

$$(E+3\Delta)(E^2-\Delta^2)-k^2(\Delta\cos 2\theta+E+2\Delta\cos^2\theta)=0, \tag{8}$$

and the eigenstates for the conduction and valence bands are given by

$$|\psi\rangle=\begin{pmatrix}\alpha'\cos\theta e^{i\phi_k}\\\gamma'\\\beta\sin\theta e^{-i\phi_k}\end{pmatrix}, \tag{9}$$

with $\alpha'=\sqrt{(E+3\Delta)/(E-\Delta)}$, $\gamma'=\sqrt{(E+\Delta\cos(2\theta)+2\Delta\cos^2\theta)/(E+\Delta)}$, and $\beta=\sqrt{(E-\Delta)/(E+3\Delta)}$.

Like the previous case, a 2Δ band-gap opening is still observed for all values of θ, but now the previous flat band no longer touches the bottom of the conduction band. In addition, the dispersion of the middle band depends on the θ parameter, being flat only when $\theta=\pi/4$ [dice lattice, Fig. 2(e)]. Note that for the specific case $\theta=0$ (graphene-like) the energy spectra for $\hat{U}_1$ [Fig. 2(a)] and $\hat{U}_2$ [Fig. 2(b)] differ only by the localization of the flat band. As we shall discuss later, this results in similar tunneling properties for both gapped cases when one-dimensional square potentials are applied to these systems.

IV. TRANSMISSION THROUGH ONE-DIMENSIONAL PERIODIC BARRIERS

First, we investigate the transmission probability of fermions in α-T_3 lattice through a finite number N of electrostatic rectangular barriers of constant height V_0, width d and interbarrier distance $s-d$, as depicted in Fig. 3. We consider both gapless and gapped cases as obtained from the presence of sublattice symmetry-breaking terms given by Eq. (5). The general Hamiltonian taking into account both the presence of the symmetry-breaking term and electrostatic potential is now given by

$$\hat{H}=\hat{H}_{\text{kin}}+V(x)\hat{I}+\Delta\hat{U}, \tag{10}$$

where $\hat{H}_{\text{kin}}$ is given by Eq. (1), $V(x)$ denotes the superlattice potential with translational symmetry breaking along the x-direction, and $\Delta\hat{U}$ represents the previous sublattice symmetry-breaking term assumed here by Eq. (5). Due to the translation invariance in the y direction the wave functions have the form $\Psi(x, y)_j = \Psi_j(x)e^{ik_y y}$, where the j index is related to the different potential regions along the x direction being outside ($j = w$) and inside ($j = b$) of the barrier. Therefore, the wave function can be written as

$$\psi_j(x) = \frac{A_j}{\sqrt{2}}\begin{pmatrix}\alpha_j\cos\theta e^{i\phi_j}\\ \gamma_j\\ \beta_j\sin\theta e^{-i\phi_j}\end{pmatrix}e^{ik_jx} + \frac{B_j}{\sqrt{2}}\begin{pmatrix}-\alpha_j\cos\theta e^{-i\phi_j}\\ \gamma_j\\ -\beta_j\sin\theta e^{i\phi_j}\end{pmatrix}e^{-ik_jx}. \tag{11}$$

The angles $\phi_j = \tan^{-1}(k_y/k_j)$ (with $j = \omega, b$) are the angles associated with the direction of the momentum of the electron in the regions inside and outside of the potential, as depicted in the insets of Fig. 3. In addition, the terms α_j, γ_j, and β_j, are obtained from the eigenstates equation using the Hamiltonian Eq. (10).

In order to obtain the transmission probability through electrostatic barriers, we need to solve the scattering problem by matching wave functions given in Eq. (11) at the interfaces inside and outside the barrier. We assume potential variations that are smooth on the length scale of the lattice constant a_0 but sharp on the scale of the Fermi wavelength $\lambda_F = 2\pi v_F/|E|$.

Writing the wave functions given by Eq. (11) in its general form as $\Psi(x) = [\psi_A(x), \psi_B(x), \psi_C(x)]^T$ and by integrating the eigenvalue equation $\hat{H}\Psi = E\Psi$ over a small interval $x = [-\epsilon, \epsilon]$, in the limit $\epsilon \to 0$, we obtain the following matching conditions for the wave function in each region

$$\psi_B(-\epsilon) = \psi_B(\epsilon), \tag{12a}$$

$$\cos\theta\psi_A(-\epsilon) + \sin\theta\psi_C(-\epsilon) = \cos\theta\psi_A(\epsilon) + \sin\theta\psi_C(\epsilon). \tag{12b}$$

Applying these matching conditions into Eq. (11), we obtain the transfer matrix for a single barrier

$$\mathcal{T}^{(1)} = \mathcal{M}_b(d)\cdot\mathcal{M}_w(0) = \begin{pmatrix} w & z\\ z* & w*\end{pmatrix}, \tag{13}$$

where $\mathcal{M}_b$ and $\mathcal{M}_w$ correspond to the transfer matrix into the well and barrier, respectively, and are given by

$$\mathcal{M}_b(d) = \Omega_{k_w}^{-1}(d)\Omega_{k_b}(d), \tag{14a}$$

$$\mathcal{M}_w(0) = \Omega_{k_b}^{-1}(0)\Omega_{k_w}(0), \tag{14b}$$

with

$$\Omega_{k_j}(x) = \begin{pmatrix}\gamma_j e^{ik_jx} & \gamma_j e^{-ik_jx}\\ \lambda_j e^{ik_jx} & -\lambda_j^* e^{-ik_jx}\end{pmatrix}, \tag{15}$$

and $\lambda_j = \alpha_j\cos^2\theta e^{i\phi_j} + \beta_j\sin^2\theta e^{-i\phi_j}$. Using Eqs. (14) and (15), one can obtain explicitly the terms w and z in Eq. (13) as

$$w = \frac{1}{a}\big[e^{-i(k_w-k_b)d}(\lambda_w^*\lambda_b^* + \eta_1\lambda_w^*\lambda_w + \eta_2\lambda_b^*\lambda_b + \lambda_w\lambda_b) + e^{-i(k_w+k_b)d}(\lambda_w\lambda_b^* - \eta_1\lambda_w^*\lambda_w - \eta_2\lambda_b^*\lambda_b + \lambda_w^*\lambda_b)\big], \tag{16a}$$

$$z = \frac{1}{a}\big[e^{-i(k_w-k_b)d}\big(\lambda_w^*\lambda_b^* - \gamma_b^2\lambda_w^*\lambda_w^* + \gamma_w^2\lambda_b^*\lambda_b - \lambda_w^*\lambda_b\big) + e^{-i(k_w+k_b)d}\big(\lambda_w^*\lambda_b + \gamma_b^2\lambda_w^*\lambda_w^* - \gamma_w^2\lambda_b^*\lambda_b - \lambda_w^*\lambda_b^*\big)\big], \tag{16b}$$

where $a = (\lambda_w^* + \lambda_w)(\lambda_b^* + \lambda_b)$, $\eta_1 = \gamma_b/\gamma_w$ and $\eta_2 = \gamma_w/\gamma_b$.

Correspondingly, the transfer matrix considering double barriers with an inter-distance s between them is

$$\mathcal{T}^{(2)} = \mathcal{M}_b(2d + s)\cdot\mathcal{M}_w(s + d)\mathcal{T}^{(1)}. \tag{17}$$

Thus, we can extend this result to N identical barriers, which is given by the product of transfer matrices:

$$\mathcal{T}^{(N)} = \prod_{l=1}^{N}\mathcal{M}_b(l(d + s) - s)\cdot\mathcal{M}_w((l - 1)(d + s)). \tag{18}$$

Once $\mathcal{T}^{(N)}$ is an unimodular matrix and the electron wave originates from the left of the system in Fig. 3, the transmission probability is obtained as $T = 1/|\mathcal{T}_{22}^{(N)}|^2$. After some algebraic calculations, we found the transmission probability through N barriers as

$$T = \frac{1}{1 + |z|^2\left(\frac{\sin N\xi}{\sin\xi}\right)^2}, \tag{19}$$

where ξ corresponds to the Bloch wave function of the whole system and is given by

$$\xi = \cos^{-1}[\mathbb{R}(w)\cos(k_w(d + s)) - \mathbb{C}(w)\sin(k_w(d + s))], \tag{20}$$

with z given by Eq. (16b), $\mathbb{R}(w)$ and $\mathbb{C}(w)$ correspond respectively to the real and imaginary terms of w in Eq. (16a).

It is important to highlight that the role of the parameter θ is built-in in the terms λ_j of the matrix in Eq. (15), such as when we assume the limiting cases $\theta = 0$ and $\theta = \pi/4$ in the term λ_j, Eq. (15) coincides with that one for dice and graphene, as discussed in Refs. [37,47].

V. TRANSMISSION OF MASSLESS DIRAC FERMIONS

Initially, we consider the symmetry-breaking free case, i.e., taking $\hat{U}_i = 0$ in Eq. (10). The solution of $\hat{H}\Psi_j = E\Psi_j$ in this case leads to $\alpha_j = \gamma_j = \beta_j = 1$, as can be seen by comparing Eqs. (11) and Eqs. (2) for the wave functions of the dispersion bands, and consequently, it implies $\eta_1 = \eta_2 = 1$ in Eq. (16a). Moreover, from the secular equation $\det(\hat{H} - E) = 0$ we obtain the wave vectors in the x direction in the well and barrier regions, k_w and k_b, respectively as

$$k_w = \sqrt{\left(\frac{E}{\hbar v_F}\right)^2 - k_y^2}\quad k_b = \sqrt{\left(\frac{E - V_0}{\hbar v_F}\right)^2 - k_y^2}, \tag{21}$$

with the eigenvalues in each region respectively given by

$$E = \pm\sqrt{\hbar^2 v_F^2\big(k_w^2 + k_y^2\big)}, \tag{22a}$$

$$E - V_0 = \pm\sqrt{\hbar^2 v_F^2\big(k_b^2 + k_y^2\big)}. \tag{22b}$$

Figure 4 shows the transmission probabilities using Eq. (19) for a single barrier as a function of the incident wave energy E and its transverse wave vector k_y for different values of the θ parameter: (a) $\theta = 0$, (b) $\theta = \pi/12$, (c)

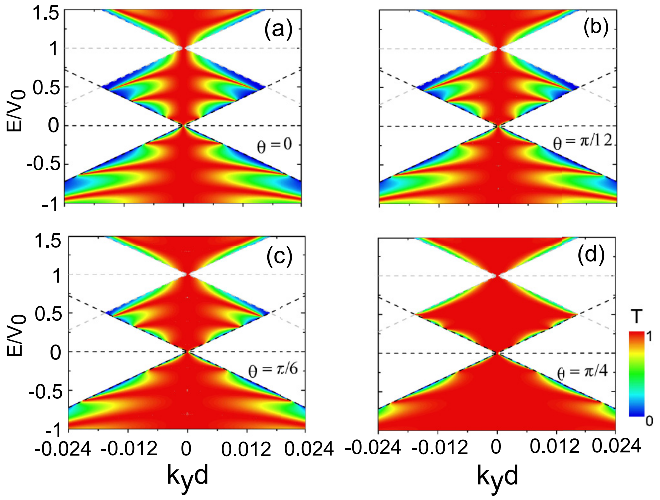

FIG. 4. Transmission probability through a single-barrier in the $(k_y, E/V_0)$ plane for (a) $\theta = 0$ (graphene-like), (b) $\theta = \pi/12$, (c) $\theta = \pi/6$, and (d) $\theta = \pi/4$ (dice) in the symmetry-breaking free case ($\hat{U} = 0$) for barrier height and width assumed as $V_0 = 0.2\,\text{eV}$ and $d = 30$ nm, respectively.

$\theta = \pi/6$, and (d) $\theta = \pi/4$. The potential height is set to $V_0 = 0.2\,\text{eV}$ and the barrier width is $d = 30$ nm. The possible non-null transmission regions in the $(k_y d, E/V_0)$ plane of Fig. 4 can be explained by identifying which modes are propagating inside and outside the potential barrier. The borders between these regions are indicated by dashed curves superimposed on the density plots, where the black and grey lines correspond to the energy spectrum outside and inside of the barrier, which are given by Eqs. (22a) and (22b), respectively. Since wave functions interfere inside the barrier, we observe for all values of θ when $E/V_0 < 1$ the appearance of resonance peaks marked by $T = 1$. In addition, when the incoming wave function is perpendicular to the barrier, the transmission is total and the barrier is completely transparent regardless of the potential width and height, as observed by the red color in the contour plots in Figs. 4 and 5 for $k_y d = 0$ and $\phi_w = 0$, respectively. This perfect transmission at normal incidence is a consequence of the conservation of the pseudo-spin at scattering on the barrier, which results in the absence of backscattering of wave functions, an effect referred as KT, which has been noted previously for the two limiting cases $\theta = 0$ [21] and $\theta = \pi/4$ [38].

We note that for $0 < E/V_0 < 0.5$ sharp resonances in the transmission probabilities become softer and less pronounced as θ increases, leading to a general enhancement trend of transmission probability for $\theta \neq 0$. This result is more evident in Fig. 5, which shows the transmission probability in the $(\phi_w, E/V_0)$ plane. We observe the broadening of transmission as θ increases in the energy region $0 < E/V_0 < 0.5$, indicating that the barrier becomes more transparent, as depicted in Fig. 6(a) for a fixed energy $E/V_0 = 0.25$. Furthermore, the special case $\theta = \pi/4$ (dice) at $E/V_0 = 0.5$ the barrier becomes fully transparent leading to an omnidirectional total transmission, as observed in Figs. 5(d) and 6(b) and discussed in Refs. [38,41].

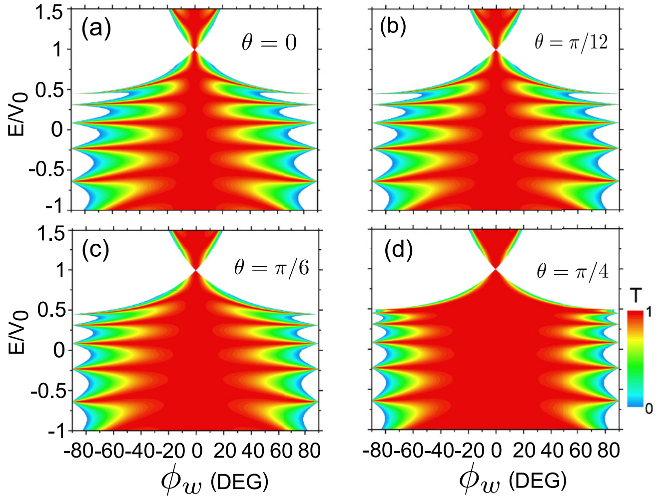

FIG. 5. Contour plot of transmission probability through a single-barrier in the $(\phi_w, E/V_0)$ plane for (a) $\theta = 0$ (graphene-like), (b) $\theta = \pi/12$, (c) $\theta = \pi/6$, and (d) $\theta = \pi/4$ (dice) for the same potential parameters as in Fig. 4.

However, as shown in Fig. 5 when the energy of incoming waves is $0.5 < E/V_0 < 1$ for all values of θ there is a reduction of the transmission probability with increasing incident energy and the transmission curves almost coincide, indicating that, analogously to the total reflection effect observed in optics, there is an incident critical angle such that above it the incident wave function is fully reflected and an evanescent wave function is found inside the potential. This angle is determined from the conservation of momentum in the y direction

$$\sin\phi_k = \frac{V_0 - E}{E}\sin\phi_q. \tag{23}$$

Since the condition for total reflection of incoming wave function is $\sin\phi_q = 1$, the incident critical angle ϕ_{kc} is determined by

$$\sin\phi_{kc} = \frac{V_0 - E}{E}. \tag{24}$$

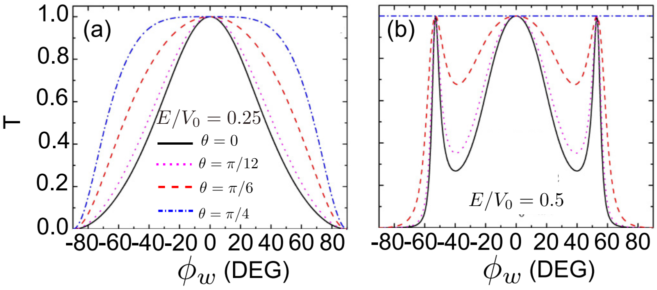

FIG. 6. Transmission probability through a single barrier as function of incident angle ϕ_w at incident energy values (a) $E/V_0 = 0.25$, and (b) $E/V_0 = 0.5$ for $\theta = 0$ (solid-black curve), $\theta = \pi/12$ (dotted-magenta curve), $\theta = \pi/6$ (dashed-red curve), and $\theta = \pi/4$ (dash-dotted-blue curve) assuming the same potential parameters as in Fig. 4.

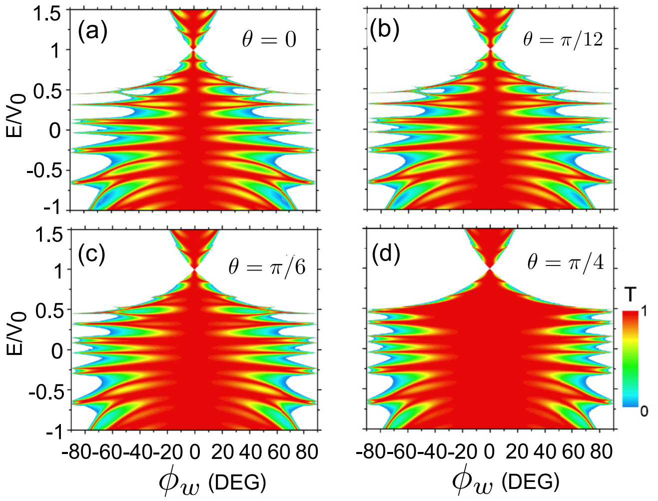

FIG. 7. Contour plot of transmission probability, shown in the $(\phi_w, E/V_0)$ plane, through a double barrier ($N = 2$) for (a) $\theta = 0$ (graphene-like), (b) $\theta = \pi/12$, (c) $\theta = \pi/6$, and (d) $\theta = \pi/4$ (dice) for the same potential parameters as in Fig. 5 and with a interbarrier distance of 30 nm.

Note that the critical angles do not depend on the parameter θ, and the transmission probabilities are almost the same for $E/V_0 > 0.5$ regardless of θ.

From Eq. (19) we analyze the effects of the number N of barriers on the transmission probabilities in the $(\phi_w, E/V_0)$ plane. The results for transmission assuming $N = 2$ and $N = 6$ are depicted in Figs. 7 and 8, respectively. For all these cases the interbarrier distance is 30 nm. One notices more resonance peaks in the transmission as the number of barriers increases as a consequence of the fact that the wave function interferes more with itself inside the barriers. Beside that, a perfect transmission $T = 1$ for normal or near-normal incidence is observed, which is a signature of the KT. Unlike graphene-like and for intermediate values of θ, the increase in the number of barriers is much less effective for dice when $0 < E/V_0 < 1$ and the SKT at $E/V_0 = 0.5$ is still observed regardless the number of barriers, as shown in Figs. 7(d) and 8(d). However, for incident energies $E/V_0 > 1$ and $E/V_0 < 0$ the effect of the number of barriers in the transmission is evident for all values of θ.

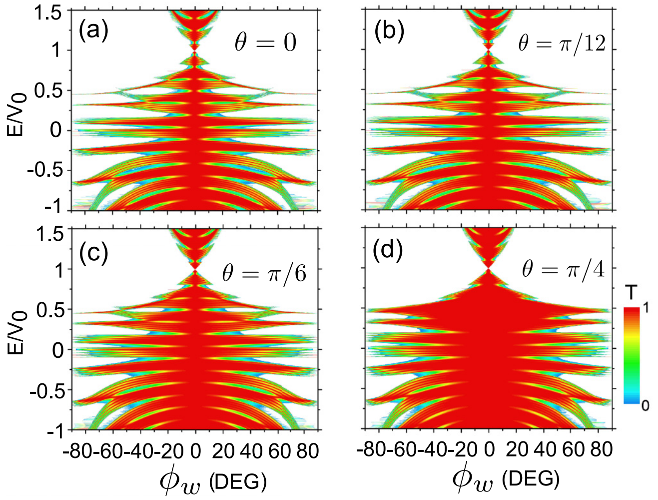

FIG. 8. The same as Fig. 7, but now for $N = 6$ barriers.

Moreover, like the single-barrier case and for $0 < E/V_0 < 0.5$, as θ increases there is a broadening of the transmission resonant peaks. Since the increase of the number of barriers does not affect the nature of pseudospin, which depends only on the crystal structure, the KT and the SKT, beside the enhancement of transmission as θ increases, are maintained regardless the number of barriers.

VI. SYMMETRY-BREAKING EFFECTS INTO THE TUNNELING PROPERTIES

As discussed in Sec. III, within the low-energy approach, the presence of small deviations in the equivalence of the atoms generate a bandgap in the energy spectrum resulting in charge carriers that are described as massive Dirac fermions. Now, we shall discuss the tunneling properties of those massive fermions in α-T_3 lattices under the presence of single and multiple barriers by considering the symmetry-breaking terms $\hat{U}_1$ and $\hat{U}_2$ given by Eq. (5).

A. Case $\hat{U} = \hat{U}_1$

Assuming $\hat{U} = \hat{U}_1$ in Eq. (10), we obtain the wave functions expressed in Eq. (11) in the barrier and well regions with $\alpha_w = \beta_w = \sqrt{E + \Delta}$, $\alpha_b = \beta_b = \sqrt{E - V_0 + \Delta}$, $\gamma_w = \sqrt{E - \Delta}$, and $\gamma_b = \sqrt{E - V_0 - \Delta}$. The schematic illustration of this junction is shown in Fig. 9. The wave vectors in the x direction inside and outside of the barrier are

$$k_w = \sqrt{\frac{E^2 - \Delta^2}{\hbar^2 v_F^2} - k_y^2}, \tag{25a}$$

$$k_b = \sqrt{\frac{(E - V_0)^2 - \Delta^2}{\hbar^2 v_F^2} - k_y^2}. \tag{25b}$$

The transmission probability is given by Eq. (19), and the terms η_1 and η_2 in Eq. (16a) are

$$\eta_1 = \sqrt{\frac{(E + \Delta)(E - V_0 - \Delta)}{(E - V_0 + \Delta)(E - \Delta)}}, \tag{26a}$$

$$\eta_2 = \sqrt{\frac{(E - \Delta)(E - V_0 + \Delta)}{(E - V_0 - \Delta)(E + \Delta)}}. \tag{26b}$$

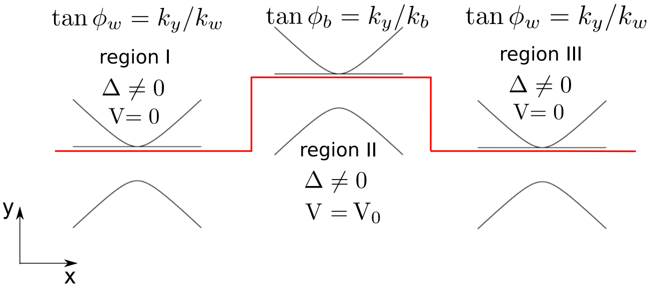

FIG. 9. Schematic illustration of the electronic energy spectrum in the α-T_3 lattice considering the inclusion of the symmetry-breaking term $\hat{U}_1$ and the square potential $V(x) = V_0\Theta(x)\Theta(d - x)$.

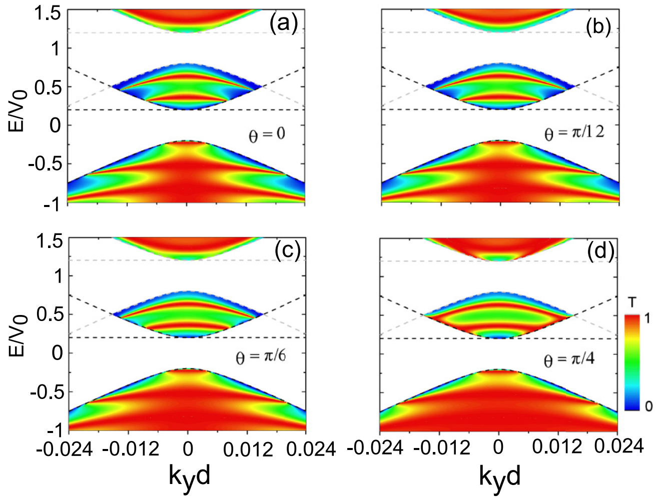

FIG. 10. Transmission probability through a single barrier in the $(k_y, E/V_0)$ plane for (a) $\theta = 0$ (graphene-like), (b) $\theta = \pi/12$, (c) $\theta = \pi/6$, and (d) $\theta = \pi/4$ (dice) by assuming the symmetry-breaking term as $\hat{U} = \hat{U}_1$, with sublattice unbalance strength $\Delta = 0.04\,\text{eV}$, for barrier height $V_0 = 0.2\,\text{eV}$ and width $d = 30$ nm.

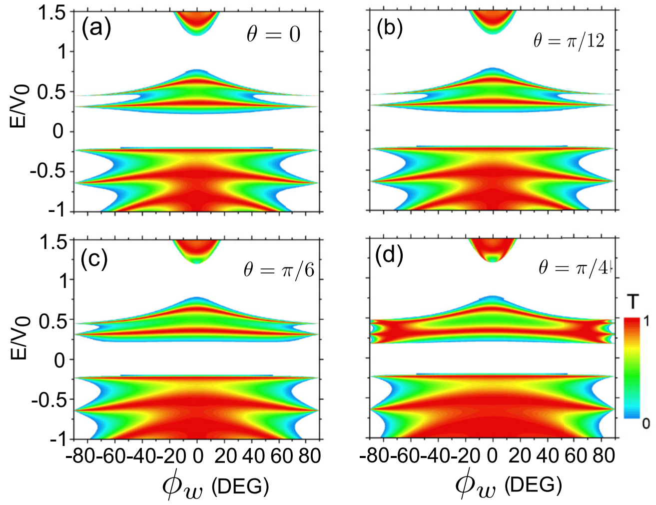

FIG. 11. Contour plot of transmission probability through a single barrier in the $(\phi_w, E/V_0)$ plane for (a) $\theta = 0$ (graphene-like), (b) $\theta = \pi/12$, (c) $\theta = \pi/6$, and (d) $\theta = \pi/4$ (dice) for the same system parameters as in Fig. 10.

The transmission probabilities for single barrier as function of $(k_yd, E/V_0)$, assuming $V_0 = 0.2\,\text{eV}$, $d = 30$ nm, and $\Delta = 0.04\,\text{eV}$ for different values of θ are shown in Fig. 10. The nonzero transmission zones are bounded by the energy levels inside and outside of barrier, corresponding to the grey and black-dashed curves, respectively. It is clearly seen that the presence of the sublattice symmetry-breaking induced bandgap in the energy spectrum lead to a suppression of the transmission for all values of the parameter θ, as well as the "fishbone" transmission shape in the energetic region $\Delta < E < 4\Delta$ is suppressed. Besides, the conservation of chirality does not take place due to the introduction of small deviation in the equivalence between the atoms and total transmission for normal or near-normal incident angles, or equivalently smaller k_yd, is no longer observed indicating that for all values of θ KT is destroyed, as depicted in Figs. 10 and 11.

However, while the KT is no longer observed, from Fig. 10(d) one notices perfect transmission when $\theta = \pi/4$ at $0 < E/V_0 < 0.5$ for large k_yd values, or equivalently for large incident angles as shown in Fig. 11(d). In fact, when θ is tuned from the correspondent value of graphene-like to dice at incident energy $E/V_0 = 0.25$ the transmission curves tend to exhibit a completely opposite feature: incident waves nearly parallel to the barrier are completely transmitted, as shown in Fig. 12(a). On the other hand, for $\theta = 0$ and oblique incident angles at incident energy $E/V_0 = 0.5$ there is a narrow resonance peak, which widens as θ increases, whereas for dice lattice beyond the broadening of this peak a new total transmission peak appears for incident angles parallel to the barrier as noticed in Fig. 12(b). The appearance of this new peak of total transmission at large values of incident angle is due to the presence of degenerate states in the electronic band structure assuming multiples barriers at energies around $E = 0.3V_0$ at large values of k_y, or equivalently to incidence angles parallel to the barrier, as shown in Fig. 15, which will be discussed further in more details.

Figure 13 shows the transmission contour plots considering now double-barrier systems with the same width and potential height used in single-barrier case and an interdistance barrier of 30 nm. Comparing to Fig. 11, we observe that beyond total reflection of waves for smaller incident angles at $E/V_0 = 0.5$, the energy scale where there is non-null transmission is reduced and for graphene-like and intermediate values of θ there is no transmission at incident energies close to the value of Δ, i.e., $E/V_0 = 0.2$. Nonetheless, for dice lattice the perfect transmission of waves near-parallel or parallel to barriers is still observed in the range $E/V_0 \in [0.2, 0.5]$ and for energies immediately above the potential energy, i.e., $1.2 < E/V_0 < 1.3$ a peak of transmission occurs for critical incident angle, like in the single-barrier case. This result is clear when we analyze the transmission curves in Fig. 14 for incident energies $E/V_0 = 1.3$ for single and double barriers. While for $\theta = \pi/4$ and $N = 1$ there is a peak of total transmission for incident

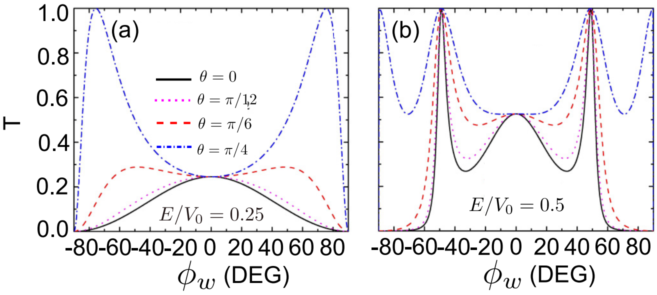

FIG. 12. Transmission probability through a single barrier as function of incident angle ϕ_w at incident energy values (a) $E/V_0 = 0.25$ and (b) $E/V_0 = 0.5$ for $\theta = 0$ (solid-black curve), $\theta = \pi/12$ (dotted-magenta curve), $\theta = \pi/6$ (dashed-red curve), and $\theta = \pi/4$ (dash-dotted-blue curve) for the same system parameters as in Fig. 10.

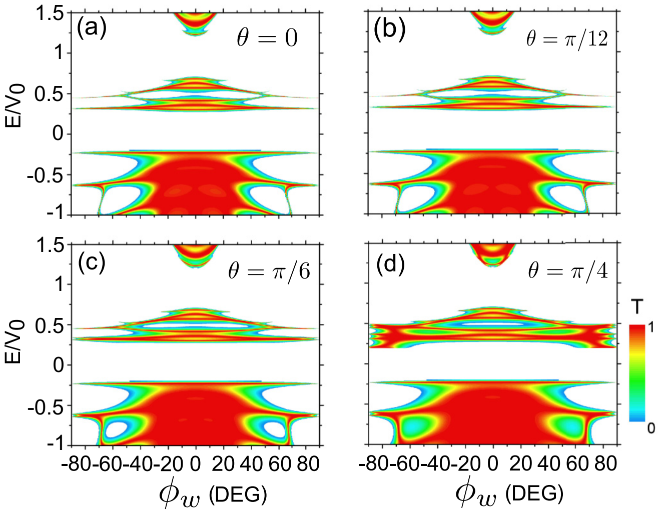

FIG. 13. Contour plot of transmission probability through a double barrier in the $(\phi_w, E/V_0)$ plane for (a) $\theta = 0$ (graphene-like), (b) $\theta = \pi/12$, (c) $\theta = \pi/6$, and (d) $\theta = \pi/4$ (dice) when $\hat{U} = \hat{U}_1$, $V_0 = 0.2\,\text{eV}$, $\Delta = 0.04\,\text{eV}$, $d = 30$ nm, and an interbarrier distance $s = 30$ nm.

angles around ±10°, which corresponds to the critical angle for this value of incident energy. For the other values of θ the transmission is reduced and falls to zero. Moreover, when $N = 2$, beyond the peak of total transmission for dice, there is a peak of almost-total transmission for $\theta = \pi/6$.

The perfect transmission at large values of $k_y d$, or incident angles parallel and near parallel to the barrier, for $\theta = \pi/4$ as observed in Figs. 11 and 12 is explained when we analyze Fig. 15(a), where we depict the electronic band structure along $k_y d$ direction of a system consisting of an infinite number of barriers with the same parameters of potential height, width, and interbarrier distance used in Fig. 13. We note that for energies at the interval $0.2 < E/V_0 < 0.5$ the minibands touch each other at large values of $k_y d$, indicating the presence of degenerate states, which is represented by prominent peaks in the density of states (DOS) at energies around $E/V_0 = 0.5$.

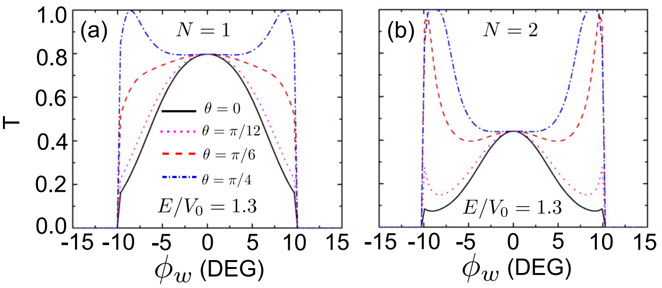

FIG. 14. Transmission probability through a (a) single barrier ($N = 1$) and (b) double barrier ($N = 2$) as function of incident angle ϕ_w at incident energy $E/V_0 = 1.3$ for $\theta = 0$ (solid-black curve), $\theta = \pi/12$ (dotted-magenta curve), $\theta = \pi/6$ (dashed-red curve), and $\theta = \pi/4$ (dash-dotted-blue curve) for the same system parameters as in Fig. 10 and an interbarrier distance of 30 nm for double barrier system.

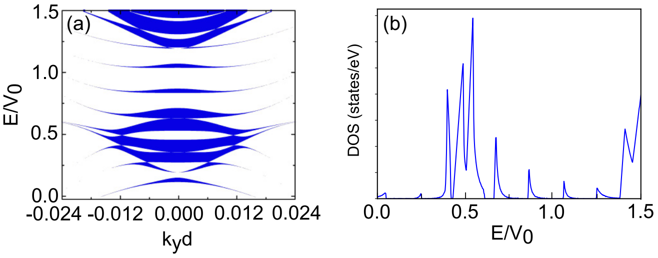

FIG. 15. (a) Electronic band structure along the $k_y d$ direction for $\theta = \pi/4$ (dice case) superlattices taking the same system parameters as in Fig. 13. (b) The corresponding DOS of (a) using Eq. (27) is shown.

The DOS was calculated using

$$D(E) = \sum_{n,k_y} \delta(E - E_{n,k_y}), \tag{27}$$

where the sums runs over all states. Therefore, since more allowed states arise for that particular energy it results in a peak in the DOS in Fig. 15(b), which leads to an enhancement of the transmission probability of electrons.

It is interesting to mention similar results were obtained considering a single potential step for the Lieb lattice in Ref. [50].

B. Case $\hat{U} = \hat{U}_2$

For the other symmetry-breaking term denoted by $\hat{U} = \hat{U}_2$ in Eq. (10), we have $\alpha_w = \sqrt{(E+3\Delta)/(E-\Delta)}$, $\alpha_b = \sqrt{(E-V_0+3\Delta)/(E-V_0-\Delta)}$, $\gamma_w = \sqrt{(E+\Delta\cos(2\theta)+2\Delta\cos^2\theta)/(E+\Delta)}$, $\gamma_b = \sqrt{(E-V_0+\Delta\cos(2\theta)+2\Delta\cos^2\theta)/(E-V_0+\Delta)}$, $\beta_w = \sqrt{E-\Delta/(E+3\Delta)}$, and $\beta_b = \sqrt{E-V_0-\Delta/(E-V_0+3\Delta)}$. This system formed by the square potential barrier and the presence of energy spectrum considering the symmetry-breaking term $\hat{U}_2$ is represented in Fig. 16.

Consequently, the wave vectors k_w and k_b are given by

$$k_w = \sqrt{\frac{(E^2-\Delta^2)(E+3\Delta)}{\hbar^2 v_F^2 (E+\Delta\cos 2\theta + 2\Delta\cos^2\theta)} - k_y^2}, \tag{28a}$$

$$k_b = \sqrt{\frac{((E-V_0)^2-\Delta^2)(E-V_0+3\Delta)}{\hbar^2 v_F^2 (E-V_0+\Delta\cos 2\theta + 2\Delta\cos^2\theta)} - k_y^2}. \tag{28b}$$

For this case, the transmission of fermions through N one-dimensional barriers is obtained using Eq. (19) with η_1 and η_2 in Eq. (16a) given by

$$\eta_1 = \sqrt{\left[\frac{E-V_0+\Delta\cos 2\theta + 2\Delta\cos^2\theta}{E+\Delta\cos 2\theta+2\Delta\cos^2\theta}\right]\eta_{12}}, \tag{29a}$$

$$\eta_2 = \sqrt{\left[\frac{E+\Delta\cos 2\theta+2\Delta\cos^2\theta}{E-V_0+\Delta\cos 2\theta + 2\Delta\cos^2\theta}\right]\eta_{21}}, \tag{29b}$$

with $\eta_{12} = \frac{E+\Delta}{E-V_0+\Delta}$ and $\eta_{21} = \frac{E-V_0+\Delta}{E+\Delta}$. The transmission probabilities as function of $(k_y d, E/V_0)$ for this case are

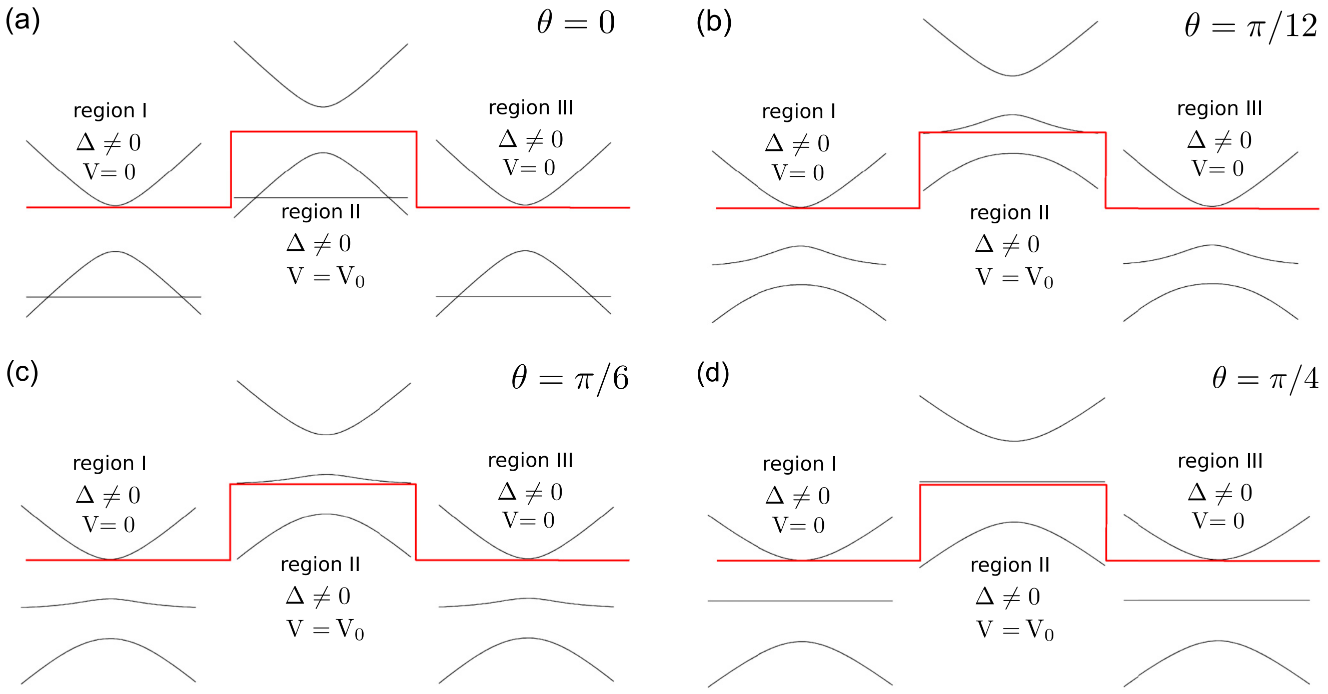

FIG. 16. Schematic illustration of the electronic energy spectrum in the α-T_3 lattice considering the inclusion of the symmetry-breaking term $\hat{U}_2$ and the square potential $V(x) = V_0\Theta(x)\Theta(d - x)$ when (a) $\theta = 0$, (b) $\theta = \pi/12$, (c) $\theta = \pi/6$, and (d) $\theta = \pi/4$.

depicted in Fig. 17. Similar to previous cases, the zones where waves are able to propagate and therefore the transmission is non-null are bounded by the energy levels inside and outside of the barrier indicated by the grey and black dashed curves superimposed on the transmission contour plot. As observed in Figs. 2(a) and 2(b), the energy spectrum for both symmetry-breaking terms $\hat{U}_1$ and $\hat{U}_2$ for $\theta = 0$ differs only by the position of the flat band maintaining the conduction and valence bands with the same dispersion and position. Since the dispersionless bands do not contribute to the transmission, the effects observed in the tunneling properties for both symmetry-breaking terms for $\theta = 0$ are similar, as noticed when we compare Figs. 17(a) and 10(a). However, for $\theta \neq 0$ the transmission contour plots are quite different from the previous gapped case, as depicted in Figs. 17(b)–17(d). We note that for incident energies $0 < E/V_0 < 1$ depending on θ new zones where there is no propagation of waves appear in the $(k_y, E/V_0)$ plane. To understand this result we plot in Fig. 18(a) diagram for the wave vector k_b inside the barrier using the relation given in Eq. (28a) for the same parameters used in Fig. 17. The blue zones indicate where the transmission is due to propagating waves, i.e., k_b is real, in that case the incoming waves might interfere with itself between the two interfaces of barrier-well, leading to the transmission resonances.

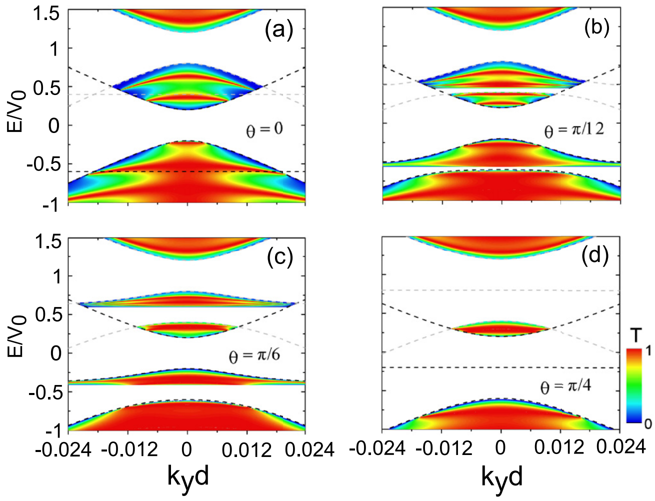

FIG. 17. Transmission probability through a single barrier in the $(k_y, E/V_0)$ plane for (a) $\theta = 0$ (graphene-like), (b) $\theta = \pi/12$, (c) $\theta = \pi/6$, and (d) $\theta = \pi/4$ (dice) when $\hat{U} = \hat{U}_2$, $V_0 = 0.2\,\text{eV}$, $\Delta = 0.04\,\text{eV}$, and $d = 30\,\text{nm}$.

When k_b is purely imaginary, indicated by the grey zone in the phase diagram, the transmission is still possible via evanescent waves but with a reduced amplitude. Furthermore, the condition to have an evanescent wave is determined by the incident critical angle, so from the conservation of momentum in the y direction and using Eq. (28) we get the expression of a critical incident angle ϕ_{kc}

$$\sin\phi_{kc} = \sqrt{E_\theta\left[\frac{((E - V_0)^2 - \Delta^2)(E - V_0 + 3\Delta)}{(E^2 - \Delta^2)(E + 3\Delta)}\right]}, \quad (30)$$

where

$$E_\theta = \frac{(E + \Delta\cos 2\theta + 2\Delta\cos^2\theta)}{(E - V_0 + \Delta\cos 2\theta + 2\Delta\cos^2\theta)}. \quad (31)$$

According to Eq. (30) and as shown in Fig. 19, unlike the gapless and previous gapped case, the critical incident angle for transmission and consequently the condition for evanescent

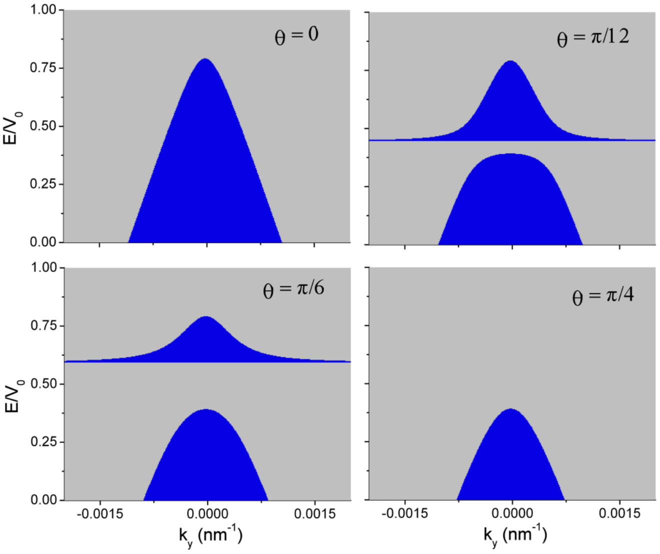

FIG. 18. Diagram obtained from the relation given in Eq. (28a) representing the wave nature inside the barrier plotted in the $(k_y, E/V_0)$ plane for (a) $\theta = 0$ (graphene-like), (b) $\theta = \pi/12$, (c) $\theta = \pi/6$, and (d) $\theta = \pi/4$ (dice) when $\hat{U} = \hat{U}_2$, $\Delta = 0.04\,\text{eV}$, $V_0 = 0.2\,\text{eV}$, and $d = 30$ nm. The blue area is the zone of propagating waves corresponding to a real wave vector k_b, the grey area is the zone where k_b is purely imaginary indicating evanescent waves.

or propagating waves depends on the value of θ, indicating the appearance of new transmission zones as θ is tuned from graphene-like to dice.

In Fig. 19 we observe at $E/V_0 = 0.25$ that while the transmission probability is nearly perfect for $\theta = \pi/12$ and $\theta = \pi/4$, for $\theta = \pi/6$ it becomes smaller, as shown in Fig. 20(a). In addition, in Fig. 20(b) we note that there is no transmission for $\theta = \pi/6$ and $\theta = \pi/4$ at $E/V_0 = 0.5$. we note that there is no transmission for $\theta = \pi/6$ and $\theta = \pi/4$ at $E/V_0 = 0.5$.

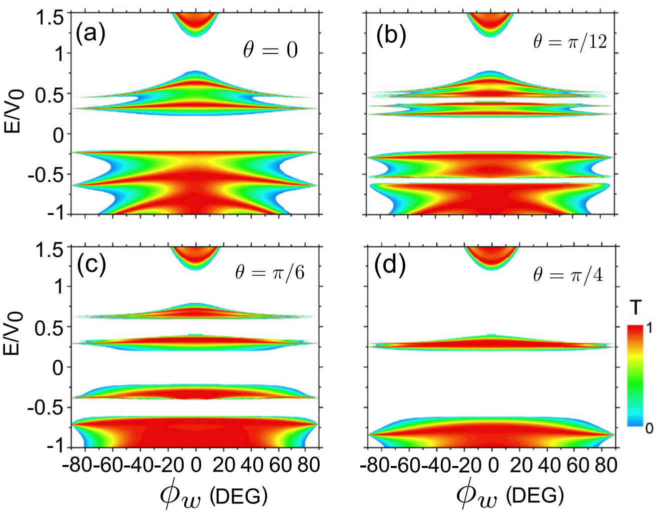

FIG. 19. Contour plot of transmission probability through a single barrier in the $(\phi_w, E/V_0)$ plane for (a) $\theta = 0$ (graphene-like), (b) $\theta = \pi/12$, (c) $\theta = \pi/6$, and (d) $\theta = \pi/4$ (dice) when $\hat{U} = \hat{U}_2$, $V_0 = 0.2\,\text{eV}$, $\Delta = 0.04\,\text{eV}$, and $d = 30$ nm.

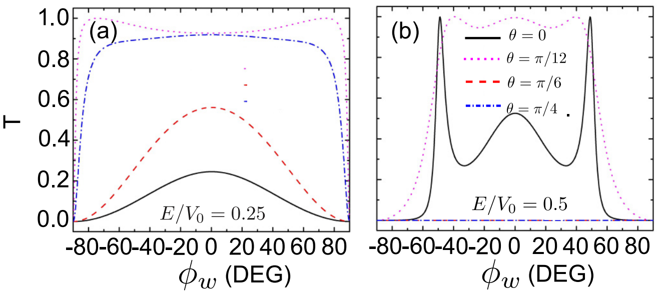

FIG. 20. Transmission probability through a single barrier as function of incident angle ϕ_w at incident energy values (a) $E/V_0 = 0.25$, and (b) $E/V_0 = 0.5$ for $\theta = 0$ (solid-black curve), $\theta = \pi/12$ (dotted-magenta curve), $\theta = \pi/6$ (dashed-red curve), and $\theta = \pi/4$ (dash-dotted-blue curve) when $\hat{U} = \hat{U}_2$, $V_0 = 0.2\,\text{eV}$, $\Delta = 0.04\,\text{eV}$, and $d = 30$ nm.

To understand these results we analyze the regions where the transmission is allowed from the diagram in Fig. 18. Where for $\theta = \pi/6$ and $\theta = \pi/4$ at $E/V_0 = 0.5$ the incident waves are localized in the grey zone of Fig. 18, and therefore are evanescent waves, and consequently the transmission is zero. On the other hand, for $\theta = \pi/12$ at this same value of incidence energy $E/V_0 = 0.5$ the transmission is almost perfect since the incident waves are propagating waves regardless the initial momentum k_y, as shown in Fig. 18(b).

Furthermore, for double-barrier systems assuming graphene-like and intermediate values of θ, the transmission is in general reduced for large incident angles and there are more resonant peaks, as shown in Fig. 21. However, for dice lattice we observe the enhancement of the transmission, which is almost perfect for all values of incident energy $0.2 < E/V_0 < 0.4$ and large values of incident angle, as shown in Fig. 21(d).

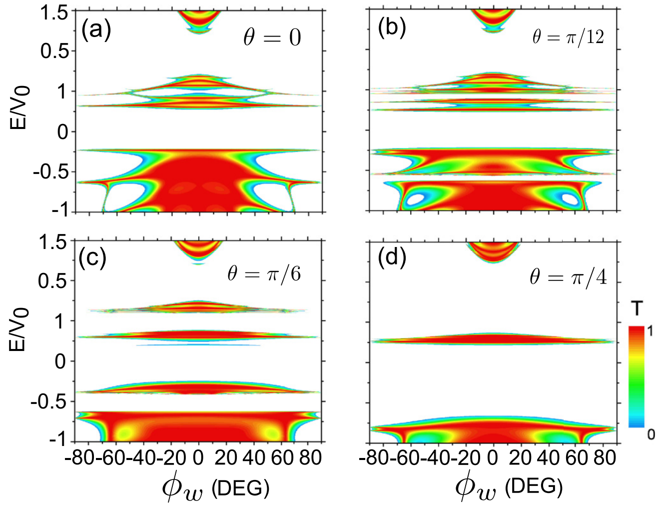

FIG. 21. Contour plot of transmission probability through a double-barrier in the $(\phi_w, E/V_0)$ plane for (a) $\theta = 0$ (graphene-like), (b) $\theta = \pi/12$, (c) $\theta = \pi/6$, and (d) $\theta = \pi/4$ (dice) when $\hat{U} = \hat{U}_2$, $V_0 = 0.2\,\text{eV}$, $\Delta = 0.04\,\text{eV}$, $d = 30$ nm, and interbarrier distance $s = 30$ nm.

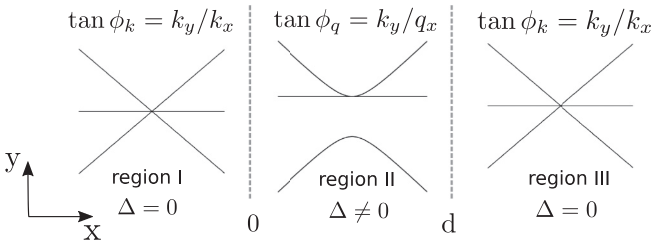

FIG. 22. Schematic illustration of the electronic energy spectrum in α-T_3 lattice at different spatial regions. In region II ($0 \leqslant x \leqslant d$), there is a bandgap in the energy spectrum induced by the presence of the symmetry-breaking term $\Delta\hat{U}_i = \hat{U}_1$.

VII. TUNNELING THROUGH SPATIAL REGIONS OF FINITE MASS

Now we investigate the tunneling properties of electrons in α-T_3 lattices when we assume a region where the electronic spectrum changes from the usual linear dispersion to a hyperbolic dispersion, due to the presence of a gap originating from the presence of the symmetry-breaking term $\hat{U}_1$, as depicted in Fig. 22. The transmission expression is obtained in a similar way as in previous section. The wave function $\Psi(x)$ corresponding to eigenstates with linear dispersion in region I and III depicted in Fig. 22 is

$$\psi(x)_{I,III} = \frac{A}{\sqrt{2}}\begin{pmatrix}\cos\theta e^{i\phi_k}\\ 1\\ \sin\theta e^{-i\phi_k}\end{pmatrix}e^{ik_x x} + \frac{B}{\sqrt{2}}\begin{pmatrix}-\cos\theta e^{-i\phi_k}\\ 1\\ -\sin\theta e^{i\phi_k}\end{pmatrix}e^{-ik_x x}. \quad (32)$$

Consequently, the wave function in region II corresponding to the hyperbolic and gapped energy spectrum at $0 \leqslant x \leqslant d$ is given by

$$\psi_{II}(x) = \frac{A'}{\sqrt{2}}\begin{pmatrix}\alpha\cos\theta e^{i\phi_q}\\ \gamma\\ \alpha\sin\theta e^{-i\phi_q}\end{pmatrix}e^{iq_x x} + \frac{B'}{\sqrt{2}}\begin{pmatrix}-\alpha\cos\theta e^{-i\phi_q}\\ \gamma\\ -\alpha\sin\theta e^{i\phi_q}\end{pmatrix}e^{-iq_x x}, \quad (33)$$

The incident angles into the different regions with linear dispersion and bandgap are $\phi_k = \tan^{-1} k_y/k_x$ and $\phi_q = \tan^{-1} k_y/q_x$, respectively, with momentum along the x direction given by

$$k_x = \sqrt{\frac{E^2}{\hbar^2 v_{\rm F}^2} - k_y^2}, \quad q_x = \sqrt{\frac{E^2 - \Delta^2}{\hbar^2 v_{\rm F}^2} - k_y^2}. \quad (34)$$

Using the matching conditions in Eq. (12) and the same procedure to get the transfer matrix in Eq. (13), we determine the transmission probability through the spatial regions of finite mass using the relation $T = 1/|\mathcal{T}_{22}^{(1)}|^2$:

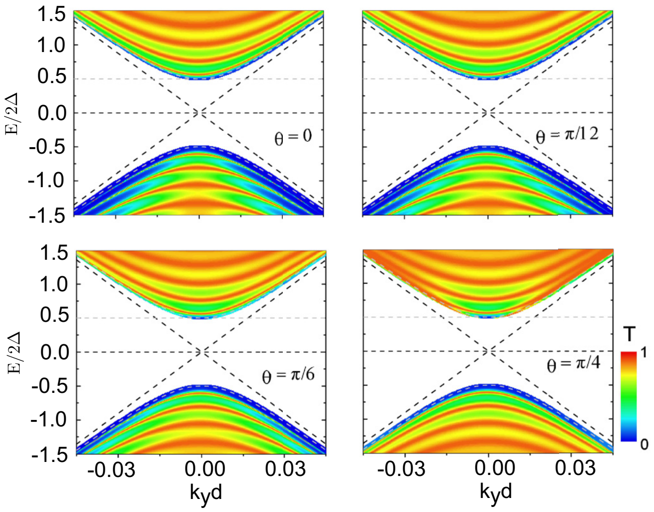

FIG. 23. Transmission contour plots as function of $k_y d$ of electrons in α-T_3 lattice through a spatial region that begins at $x = 0$ and width $d = 30$ nm where there is a bandgap 2Δ in the energy spectrum induced by the presence of the symmetry-breaking term $\Delta\hat{U}_i = \hat{U}_1$ with $\Delta = 0.1$eV and for (a) $\theta = 0$, (b) $\theta = \pi/12$, (c) $\theta = \pi/6$, and (d) $\theta = \pi/4$.

$$T = \frac{1}{a_k a_q}[e^{i(k_x+q_x)d}(\Lambda_k\Lambda_q^* - \eta_1\Lambda_k\Lambda_k^* - \eta_2\Lambda_q\Lambda_q^* + \Lambda_k^*\Lambda_q) + e^{i(k_x-q_x)d}(\Lambda_k\Lambda_q + \eta_1\Lambda_k\Lambda_k^* + \eta_2\Lambda_q\Lambda_q^* + \Lambda_k^*\Lambda_q^*)], \quad (35)$$

where $\Lambda_j = \cos^2\theta e^{\phi_j} + \sin^2\theta e^{-\phi_j}$, $a_j = \Lambda_j + \Lambda_j^*$ with $j = k$ and $j = q$ denoting the linear energy spectrum and gapped regions, respectively. In that case $\eta_1 = \sqrt{(E-\Delta)/(E+\Delta)}$ and $\eta_2 = \sqrt{(E+\Delta)/(E-\Delta)}$.

Figure 23 shows the transmission probabilities plotted in the $(k_y d, E/2\Delta)$ plane for different θ, using $d = 30$ nm, and $\Delta = 0.1$ eV, resulting in a bandgap opening of $2\Delta = 0.2$ eV into region II. Since our motivation is to compare the transmission results obtained in this section to the previous one assuming transmission through potential barriers, here we assume a bandgap with the same energy of that height of potential used in the previous sections.

The energy spectrum in the different regions, i.e., in the region with linear dispersion and in the region with hyperbolic dispersion are indicated by dashed curves superimposed on the contour plots. We note that due to the band-gap opening in region II, when incident energies are inside the gap $-0.1 < E < 0.1$ the transmission is exponentially small and for $k_y d = 0$ the transmission $T < 1$. Unlike the case of tunneling through barriers discussed in Sec. V, there is absence of KT. Moreover, beyond the enhancement of the transmission as θ increases, the transmission curves are almost the same as incident energy increases only for smaller incident angles ϕ_k, as observed in Fig. 24. From Fig. 24 we observe, in general, that there is a broadening of transmission curves for greater values of θ, like the barrier system case. However, for ener-

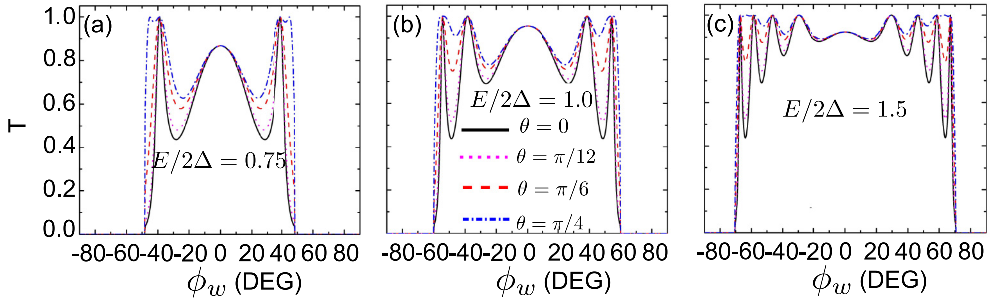

FIG. 24. Transmission probability as function of incident angle ϕ_k, and incident energy (a) $E = 0.15$ eV, (b) $E = 0.20$ eV, (c) $E = 0.30$ eV for $\theta = 0$ (solid-black curve), $\theta = \pi/12$ (dotted-magenta curve), $\theta = \pi/6$ (dashed-red curve), and $\theta = \pi/4$ (dash-dotted-blue curve) when $\hat{U} = \hat{U}_1$ in the region II in Fig. 22 with $\Delta = 0.1$ eV and $d = 30$ nm.

gies $E < 2\Delta$, which is analogous to incident energies bellow the potential barrier in the previous sections, the number of peaks in the transmission curves is the same regardless of the parameter θ, as shown in Fig. 24(a). In addition, the transmission continues to be enhanced even for incident energy above the band-gap energy 2Δ, as represented in Figs. 24(b) and 24(c). This result is opposite to the one observed for tunneling through potential barriers, where the transmission is reduced for energies above the one associated to the critical angle. Besides, the difference between the transmission curves as θ is tuned from graphene-like to dice is more evident for values $E > 2\Delta$, as shown in Fig. 24(c), where for $\theta = \pi/4$ the transmission curve is more smooth for larger values of ϕ_k.

VIII. CONCLUSIONS

In summary, using the transfer matrix approach, we investigated the tunneling properties in α-T_3 lattices of electrons across square barriers and through regions of space where the energy spectrum has a finite bandgap. For tunneling across one-dimensional square barriers, we consider both the case of equivalence between the three sublattices, and the ones where bandgaps originate due to small deviations of this equivalence by including symmetry-breaking terms. We also investigated tunneling of electrons from regions with a linear to a hyperbolic dispersion.

For the massless Dirac fermion case, when no symmetry-breaking terms are present, besides a general trend of enhanced transmission with increasing α, KT at normal incidence is found for all values of θ, regardless the number of barriers. At oblique incidence, the transmission increases with increasing θ. For a particular case, $E/V_0 = 0.5$ and $\theta = \pi/4$ (dice), an omnidirectional transmission is observed, which is called *super-Klein tunneling* (SKT) effect, and preserved regardless of the number of barriers. Although the increase in the number of barriers gives rise to additional resonances in the transmission for all values of θ, this increase is much less pronounced for the dice lattice, whereas for a graphene-like lattice the transmission probability is strongly modified. Moreover, we found that, similar to total reflection in optics, above an incident angle ϕ_k there is total reflection of the incident wave functions. This critical angle depends only on the incident energy and potential barrier and remains the same for all values of θ. Our findings concerning the robustness of the omnidirectional transmission observed at $E = 0.5V_0$ for the dice lattice was also predicted in Ref. [40] using the WKB method.

The presence of an additional symmetry-breaking term in the Hamiltonian distorts the linear dispersion around the Dirac point and changes the location of the flat band, whose occurrence depends on the deviation of the equivalence between the three sublattices. The symmetry-breaking term destroys the KT and SKT in the α-T_3 model. It is demonstrated that the additional term in general suppresses the transmission probabilities for both cases $\hat{U}_1$ and $\hat{U}_2$. When the flat band is located at the band edge, i.e., when $\hat{U}_1 = \mathrm{diag}(1, -1, 1)$, resonant tunneling is considerably suppressed and at incident energies $0 < E/V_0 < 0.5$ the transmission is perfect for larger values of incident angle, as a consequence of the presence of degenerate states around large values of k_y observed from the electronic band structure. In addition, when we consider the double-barrier system at $E/V_0 = 0.5$, unlike the single barrier, the transmission is reduced for smaller ϕ_w, and perpendicular or near-perpendicular incident wave functions are totally reflected.

When $\hat{U}_2 = \mathrm{diag}(1, -1, -3)$, since the nature of wave vector k_b inside the potential depends on the coupling parameter we note that for $0 < E/V_0 < 1$ and intermediate values of θ new zones with total reflection of the wave function appears as θ is tuned from graphene-like to dice, indicating the strong relation between the transmission properties and both location and distortion of the energy band inside the gap. However, the transmission probabilities are much less affected by an increase of the number of barriers as θ increases.

We also discussed the tunneling properties of electrons in α-T_3 lattices when they traverse a region of space where the spectrum exhibits a finite energy gap. In the case we considered here, the gap is induced by inclusion of a symmetry-breaking term $\hat{U}_1$, rendering the sublattice C nonequivalent. The consequence is the opening of a gap in the energy spectrum. We have shown that the existence of an energy gap prevents the KT and SKT from taking place for all values of θ, and the transmission for perpendicular or near-perpendicular waves are less than 1, unlike the transmission through a potential barrier. Moreover, at larger values of incident energy we noted a broadening of the transmission curves as θ increases. For dice the transmission peaks are smoothed as incident energy increases, and at large incident angles the transmission is perfect as a consequence of degenerate states at large values of k_y, as observed in the potential barrier case when the $\hat{U}_1$ term was considered.

The results obtained in this paper are useful to understand the effects in the transmission properties due to small deviations in the equivalence between the three sublattices in α-T_3 lattices, as well as the role of location and dispersion of the band inside the gap in the occurrence of KT and SKT. We discussed a versatile engineering to control and prevent the SKT and KT, which is a necessary condition for nanoelectronic applications, by changing the symmetry between the atomic sites of the crystal and consequently, controlling the dispersion of the middle band.

ACKNOWLEDGMENTS

This study was financed in part by the National Council for the Improvement of Higher Education (CAPES) of Brazil through CAPES/PRINT, Finance Code No. 88887.508174/2020-00, and financial support through the University of Antwerp for S.M.C., and the Flemish Science Foundation (FWO-Vl) through a postdoc fellowship for B.V.D. D.R.C. is supported by CNPq Grants No. 310019/2018-4 and No. 437067/2018-1.

---

[1] P. Markoš and C. M. Soukoulis, *Wave Propagation: From Electrons to Photonic Crystals and Left-Handed Materials* (Princeton University Press, Princeton, 2008).

[2] P. A. M. Dirac, The quantum theory of the electron, Proc. R. Soc. London **117**, 610 (1928).

[3] O. Klein, Die Reflexion von Elektronen an einem Potentialsprung nach der relativistischen Dynamik von Dirac, Z. Phys. **53**, 157 (1929).

[4] N. Dombey, A. Calogeracos, Seventy years of the Klein paradox, Phys. Rep. **315**, 41 (1999).

[5] B. H. J. McKellar and G. J. Stephenson, Jr., Relativistic quarks in one-dimensional periodic structures, Phys. Rev. C **35**, 2262 (1987).

[6] M. I. Katsnelson, K. S. Novoselov, and A. K. Geim, Chiral tunnelling and the Klein paradox in graphene, Nat. Phys. **2**, 620 (2006).

[7] V. V. Cheianov and V. Falko, Selective transmission of Dirac electrons and ballistic magnetoresistance of $n-p$ junctions in graphene, Phys. Rev. B **74**, 041403(R) (2006).

[8] J. M. Pereira, V. Mlinar, F. M. Peeters, and P. Vasilopoulos, Confined states and direction-dependent transmission in graphene quantum wells, Phys. Rev. B **74**, 045424 (2006).

[9] B. Huard, J. A. Sulpizio, N. Stander, K. Todd, B. Yang, and D. Goldhaber-Gordon, Transport Measurements Across a Tunable Potential Barrier in Graphene, Phys. Rev. Lett. **98**, 236803 (2007).

[10] R. V. Gorbachev, A. S. Mayorov, A. K. Savchenko, D. W. Horsell, and F. Guinea, Conductance of *p-n-p* graphene structures with "air-bridge" top gates, Nano Lett. **8**, 1995 (2008).

[11] N. Stander, B. Huard, and D. Goldhaber-Gordon, Evidence for Klein Tunneling in Graphene $p-n$ Junctions, Phys. Rev. Lett. **102**, 026807 (2009).

[12] A. F. Young and P. Kim, Quantum interference and Klein tunnelling in graphene heterojunctions, Nat. Phys. **5**, 222 (2009).

[13] K. S. Novoselov, A. K. Geim, S. V. Morozov, D. Jiang, Y. Zhang, S. V. Dubonos, I. V. Grigorieva, and A. A. Firsov, Electric field effect in atomically thin carbon films, Science **306**, 666 (2004).

[14] S. V. Morozov, K. S. Novoselov, M. I. Katsnelson, F. Schedin, D. C. Elias, J. A. Jaszczak, and A. K. Geim, Giant Intrinsic Carrier Mobilities in Graphene and Its Bilayer, Phys. Rev. Lett. **100**, 016602 (2008).

[15] E. B. Sonin, Effect of Klein tunneling on conductance and shot noise in ballistic graphene, Phys. Rev. B **79**, 195438 (2009).

[16] L. P. Miranda, S. P. Milovanović, R. N. Costa Filho, and F. M. Peeters, Hall and bend resistance of a phosphorene Hall bar, Phys. Rev. B **104**, 035401 (2021).

[17] T. M. Rusin and W. Zawadzki, Zitterbewegung of electrons in graphene in a magnetic field, Phys. Rev. B **78**, 125419 (2008).

[18] W. Zawadzki and T. M. Rusin, Zitterbewegung (trembling motion) of electrons in semiconductors: A review, J. Phys.: Condens. Matter **23**, 143201 (2011).

[19] S. M. Cunha, D. R. da Costa, G. O. de Sousa, Andrey Chaves, J. Milton Pereira, Jr., and G. A. Farias, Wave-packet dynamics in multilayer phosphorene, Phys. Rev. B **99**, 235424 (2019).

[20] I. R. Lavor, D. R. da Costa, Andrey Chaves, S. H. R. Sena, G. A. Farias, B. Van Duppen and F. M. Peeters, Effect of Zitterbewegung on the propagation of wave packets in ABC-stacked multilayer graphene: An analytical and computational approach, J. Phys.: Condens. Matter **33**, 095503 (2021).

[21] P. E. Allain and J. N. Fuchs, Klein tunneling in graphene: Optics with massless electrons, Eur. Phys. J. B **83**, 301 (2011).

[22] J. M. Pereira Jr, F. M. Peeters, A. Chaves, and G. A. Farias, Klein tunneling in single and multiple barriers in graphene, Semicond. Sci. Technol. **25**, 033002 (2010).

[23] A. Raoux, M. Morigi, J.-N. Fuchs, F. Piéchon, and G. Montambaux, From Dia- to Paramagnetic Orbital Susceptibility of Massless Fermions, Phys. Rev. Lett. **112**, 026402 (2014).

[24] M. Slot, T. Gardenier, P. Jacobse, G. C. P. van Miert, S. N. Kempkes, S. J. M. Zevenhuizen, C. M. Smith, D. Vanmaekelbergh, and I. Swart, Experimental realization and characterization of an electronic Lieb lattice, Nat. Phys. **13**, 672 (2017).

[25] Z. Li, J. Zhuang, L. Chen, L. Wang, H. Feng, X. Xu, X. Wang, C. Zhang, K. Wu, S. X. Dou *et al.*, Realization of flat band with possible nontrivial topology in electronic Kagome lattice, Sci. Adv. **4**, eaau4511 (2018).

[26] S. Borisenko, Q. Gibson, D. Evtushinsky, V. Zabolotnyy, B. Büchner, and R. J. Cava, Experimental Realization of a Three-Dimensional Dirac Semimetal, Phys. Rev. Lett. **113**, 027603 (2014).

[27] Z. K. Liu, B. Zhou, Y. Zhang, Z. J. Wang, H. M. Weng, D. Prabhakaran, S.-K. Mo, Z. X. Shen, Z. Fang, X. Dai *et al.*, Discovery of a three-dimensional topological Dirac semimetal, Na_3Bi, Science **343**, 864 (2014).

[28] B. Dóra, J. Kailasvuori, and R. Moessner, Lattice generalization of the Dirac equation to general spin and the role of the flat band, Phys. Rev. B **84**, 195422 (2011).

[29] B. Sutherland, Localization of electronic wave functions due to local topology, Phys. Rev. B **34**, 5208 (1986).

[30] E. H. Lieb, Two Theorems on the Hubbard model, Phys. Rev. Lett. **62**, 1201 (1989).

[31] J. D. Malcolm and E. J. Nicol, Magneto-optics of general pseudospins two-dimensional Dirac-Weyl fermions, Phys. Rev. B **90**, 035405 (2014)

[32] Z. Lan, N. Goldman, A. Bermudez, W. Lu, and P. Öhberg, Dirac-Weyl fermions with arbitrary spin in two-dimensional optical superlattices, Phys. Rev. B **84**, 165115 (2011)

[33] L. Wang and D.-X. Yao, Coexistence of spin-1 fermion and Dirac fermion on the triangular kagome lattice, Phys. Rev. B **98**, 161403(R) (2018).

[34] E. Illes, Properties of the α-T_3 Model, Ph.D. thesis, University of Guelph, Canada, 2017.

[35] A. Iurov, G. Gumbs, and D. Huang, Peculiar electronic states, symmetries, and Berry phases in irradiated α-T_3 materials, Phys. Rev. B **99**, 205135 (2019).

[36] Y. Xie, Y. Tan, and A. W. Ghosh, Spintronic signatures of Klein tunneling in topological insulators, Phys. Rev. B **96**, 205151 (2017).

[37] Y. Xu and G. Jin, Omnidirectional transmission and reflection of pseudospin-1 Dirac fermions in a Lieb superlattice, Phys. Lett. A **378**, 3554 (2014).

[38] D. F. Urban, D. Bercioux, M. Wimmer, and W. Häusler, Barrier transmission of Dirac-like pseudospin-one particles, Phys. Rev. B **84**, 115136 (2011).

[39] C.-Y. Tan, C.-X. Yan, Y.-H. Zhao, H. Guo, and H.-R. Chang, Anisotropic longitudinal optical conductivities of tilted Dirac bands in $1T' - MoS_2$, Phys. Rev. B **103**, 125425 (2021).

[40] N. Weekes, A. Iurov, L. Zhemchuzhna, G. Gumbs, and D. Huang, Generalized WKB theory for electron tunneling in gapped α-T_3 lattices, Phys. Rev. B **103**, 165429 (2021).

[41] E. Illes and E. J. Nicol, Klein tunneling in the α-T_3 model, Phys. Rev. B **95**, 235432 (2017).

[42] V. G. Veselago, The electrodynamics of substances with simultaneously negative values of ϵ and μ, Sov. Phys. Usp. **10**, 509 (1968).

[43] J. B. Pendry, Positively negative, Nature (London) **423**, 22 (2003).

[44] V. V. Cheianov, V. Falko, and B. L. Altshuler, The focusing of electron flow and a Veselago lens in graphene $p - n$ junctions, Science **315**, 1252 (2007).

[45] L. Mandhour and F. Bouhadida, Klein tunneling in deformed α-T_3 lattice, arXiv:2004.10144.

[46] C. H. Yang, R. Wieser, and L. Wang, The effect of a variable coupling parameter on the tunneling properties from graphene to α-T_3 model, J. Appl. Phys. **128**, 094301 (2020).

[47] M. Barbier, F. M. Peeters, P. Vasilopoulos, and J. Milton Pereira, Jr., Dirac and Klein-Gordon particles in one-dimensional periodic potentials, Phys. Rev. B **77**, 115446 (2008).

[48] S. M. Cunha, D. R. da Costa, J. Milton Pereira, Jr., R. N. Costa Filho, B. Van Duppen, and F. M. Peeters, Band-gap formation and morphing in α-T_3 superlattices, Phys. Rev. B **104**, 115409 (2021).

[49] J. Viana Gomes and N. M. R. Peres, Tunneling of Dirac electrons through spatial regions of finite mass, J. Phys.: Condens. Matter **20**, 325221 (2008).

[50] Y. Betancur-Ocampo, G. Cordourier-Maruri, V. Gupta, and R. de Coss, Super-Klein tunneling of massive pseudospin-one particles, Phys. Rev. B **96**, 024304 (2017).